MDPI

Article

Analysis of Chaotic Features in Dry Gas Seal Friction State Using Acoustic Emission

Shuai Zhang [1], Xuexing Ding [1], Jinlin Chen [1,*], Shipeng Wang [2] and Lanxia Zhang [1]

[1] College of Petrochemical Engineering, Lanzhou University of Technology (LUT), Lanzhou 730050, China; 221080706003@lut.edu.cn (S.Z.); dingxxseal@126.com (X.D.); 211080706001@lut.edu.cn (L.Z.)
[2] State Key Laboratory of Tribology in Advanced Equipment, Department of Mechanical Engineering, Tsinghua University, Beijing 100084, China; sp-wang@mail.tsinghua.edu.cn
[*] Correspondence: jinlinchen119@163.com

Abstract: In this study, a chaos theory-based characterization method is proposed to address the nonlinear behavior of acoustic emission (AE) signals during the startup and shutdown phases of dry gas seals. AE signals were collected through a controlled experiment at three distinct phases: startup, normal operation, and shutdown. Analysis of these signals identified a transition speed of 350 r/min between the mixed lubrication (ML) and hydrodynamic lubrication (HL) states. The maximum Lyapunov exponent, correlation dimension, K-entropy, and attractors of the AE signals throughout the operation of the dry gas seal are calculated and analyzed. The findings indicate that the chaotic features of these signals reflect the friction state of the seal system. Specifically, when the maximum Lyapunov exponent is greater than zero, the system exhibits chaotic behavior. The correlation dimension and K-entropy first increase and then decrease in boundary and hybrid lubrication states, while remaining stable in the hydrodynamic lubrication state. Attractors exhibit clustering in boundary lubrication and dispersion in mixed lubrication states. The proposed method achieves an accuracy of 98.6% in recognizing the friction states of dry gas seals. Therefore, the maximum Lyapunov exponent, correlation dimension, and K-entropy are reliable tools for characterizing friction states, while attractors serve as a complementary diagnostic feature. This approach provides a novel framework for utilizing AE signals to evaluate the friction states of dry gas seals.

Keywords: dry gas seals; chaos theory; acoustic emission; friction state

1. Introduction

Dry gas seals, renowned for their exceptional performance, are widely employed in critical applications, including centrifugal compressors [1], aircraft engines, and nuclear power pumps. As these technologies evolve to operate at higher speeds and pressures, the integrity and stability of dry gas seals are increasingly challenged. This growing concern underscores the need for a deep understanding of the dynamics governing the friction states of dry gas seals, which is crucial for their optimal operation and maintenance.

The conventional destructive monitoring approach, which involves embedding sensors in the static ring, often compromises seal performance and compatibility [2]. In contrast, advanced nondestructive acoustic emission (AE) technology offers a transformative solution for real-time monitoring of dry gas seal conditions, providing superior potential compared to traditional methods [3,4]. Early work in AE monitoring, beginning in 1969 with Orcutt's exploration of its effectiveness in evaluating mechanical seals [5], was further advanced by Miettinen in 1995, who applied AE techniques to analyze the sliding contact

behavior of seals [6]. Today, AE technology is recognized for its exceptional capability in acting as a highly sensitive indicator of lubrication conditions, serving as a foundation for condition monitoring in various systems, including bearings and gearboxes [7–9].

AE technology's high sensitivity and resolution make it an effective tool for detecting subtle changes in the operating conditions of mechanical systems. AE sensors detect stress wave signals generated by friction on the seal end face. Huang et al. [10] analyzed the frequency bands associated with friction during the startup and shutdown phases of dry gas seals, while Xu et al. [11] studied AE signals across three operational states: non-contact, light contact, and excessive contact. Sun et al. [12] employed the SVD–AVMD method to extract AE characterization signals related to the friction state of liquid film seals, and Towsyfyan et al. [13] explored AE characterization of typical faults in mechanical seals. Li et al. [14] utilized genetic particle filters and support vector machine signal analysis for mechanical seal fault classification. Despite their potential, AE-based monitoring methods have limitations, such as complex interpretation and susceptibility to ambient noise, which can lead to false positives or negatives.

To overcome these challenges, chaos theory offers a promising approach for feature extraction from AE signals, leveraging the high sensitivity of chaotic systems to initial conditions and their complex dynamical behavior. Chaos theory has been successfully applied to machine condition monitoring and fault diagnosis. Zhu et al. [15] demonstrated that friction signals exhibit a broad continuous power spectrum, fractal dimension, and maximum Lyapunov exponent, confirming the chaotic nature of friction systems. Sun et al. [16] used chaotic attractor phase trajectories to characterize the chaotic properties and evolution patterns of friction vibration signals during grinding. Lewis et al. [17] explored methods for extracting weak signals from chaotic backgrounds, while Ziaja et al. [18] applied chaos theory to diagnose rolling bearing faults. Despite the promise of chaos theory, its application in dry gas seals remains underexplored. Based on our review of the current state of research in the world's leading scientific centers, we observe that the judgment of the friction state in dry gas seals largely relies on empirical methods rather than specific characteristic indicators.

Existing studies have shown a strong correlation between seal operating conditions and the root mean square (RMS) value of AE signals, highlighting the effectiveness of chaos theory as a framework for understanding mechanical operating conditions. However, the friction state features of dry gas seal end faces have not been thoroughly investigated. This study aims to address this gap by proposing an experimental investigation that employs chaos theory as an analytical tool to determine the state features of the seal end face. The goal is to provide valuable insights and methods for the effective identification and fault diagnosis of dry gas seal states in future applications.

2. Theoretical Analysis

In studying the start–stop phase of a dry gas seal, traditional linear analysis methods often fail to capture subtle changes in system behavior because of inherent nonlinearity and complexity. Chaos theory provides a powerful framework for uncovering and understanding the system's complex dynamics, thereby enhancing its ability to predict and control its behavior. The chaos indicators employed in this study, including the Lyapunov exponent and fractal dimension, are particularly effective in reflecting the system's stability and complexity. These indicators are highly sensitive, which allows them to detect minor variations that traditional methods—such as linear regression or time series analysis—may miss. In comparison with other analytical methods commonly utilized in related studies, including Fourier transform or wavelet analysis, chaos theory stands out by effectively revealing both short-term dynamics and long-term behavioral patterns. The literature

review reports that numerous studies rely exclusively on linear models, which can result in misinterpretations of system behavior. By contrast, the developed approach offers a more comprehensive understanding of the underlying dynamics.

2.1. Phase-Space Reconstruction

The first step in analyzing time series signals of chaotic systems is the reconstruction of phase-space, which is a crucial tool for understanding the system's evolution and dynamics. In the study of dynamical systems, phase-space is conceptualized as a multidimensional domain generated by expanding the states or dimensions of the system's variables. This reconstruction is crucial for unraveling the complex behaviors characteristic of chaotic systems. Using the delayed coordinate method, Takens [19] introduced the phase-space reconstruction of a chaotic time series.

$$X = \left\{ X_i \middle| X_i = \left[x_i, x_{i+\tau}, \cdots, x_{i+(m-1)\tau} \right], i = 1, 2, \cdots, M \right\} \tag{1}$$

where m is the embedding dimension, τ is the delay time, N is the series length, and M is the number of vectors in phase-space, with $M = N - (m-1)\tau$. Takens' theorem provides a basis for selecting the embedding dimension under the assumption of a long and noise-free time series. Nonetheless, because actual time series data are finite and noisy, the appropriate embedding dimension m and delay time τ must be carefully chosen.

Currently, two perspectives on the selection of m and τ exist. One perspective is that these methods operate independently, as shown by approaches including the autocorrelation method [20] and the mutual information method [21] for determining time delay, as well as the G–P algorithm [22] and the FNN method [23] for determining the embedding dimension. The other perspective suggests that m and τ are related, as supported by approaches including the embedding window method [24] and the C–C method [25].

The C–C method can simultaneously determine both the optimal delay time and the embedding dimension of a time series employing correlation integrals. Before calculation, several parameters must be specified. τ_s is the sampling interval of the time series, and τ denotes the delay time. The actual delay time for the time series is expressed as $\tau_d = \tau \tau_s$, and the delay time window is designated as τ_w. By analyzing the statistical properties, the appropriate delay time τ_s can be accurately calculated, which then determines the time window τ. Finally, the embedding dimension m is derived on the basis of the combination of the time window τ_w and the determined time series delay time τ_d.

Using the formula provided in Equation (1), the correlation integral for the embedded time series is calculated. This formula offers a quantitative measure of the relationship between the embedded points in phase-space.

$$C(m, N, r, t) = \frac{2}{M(M-1)} \sum_{1 \leq i \leq j \leq M} \theta(r - \|X_i - X_j\|), r > 0 \tag{2}$$

where $\theta(x) = 0$, if $x < 0$, and $\theta(x) = 1$, if $x \geq 0$. The correlation integral is a cumulative distribution function that represents the probability that the distance between any two points in the phase–space is less than r.

Define the test statistic:

$$S_1(m, N, r, t) = C(m, N, r, t) - C^m(1, N, r, t) \tag{3}$$

The time series can be first divided into t disjoint subsequences, where t is a natural number smaller than 200 in practical calculations.

$$\{x_1, x_{t+1}, x_{2t+1}, \cdots\}$$
$$\{x_2, x_{t+2}, x_{2t+2}, \cdots\}$$
$$\cdots\cdots\cdots\cdots\cdots\cdots$$
$$\{x_t, x_{2t}, x_{3t}, \cdots\} \tag{4}$$

Using the strategy of chunked averaging, the statistics defined in Equation (3) are calculated.

$$S_2(m, N, r, t) = \frac{1}{t}\sum_{s=1}^{t}[C_s(m, \frac{N}{t}, r, t) - C_s^m(1, \frac{N}{t}, r, t)] \tag{5}$$

When $N \to \infty$,

$$S_2(m, r, t) = \frac{1}{t}\sum_{s=1}^{t}[C_s(m, r, t) - C_s^m(1, r, t)] \tag{6}$$

If the time series were independent and identically distributed, then $N \to \infty$ and $S_2(m, r, t) = 0$ for all r and fixed m and t. However, in practice, the series is finite, and its elements may be interrelated, which leads to $S_2(m, r, t) \neq 0$. Therefore, the zero point of $S_2(m, r, t)$ or the time point of the minimum difference between each time point across all radii r can be utilized to identify the local maximum time interval t, with these points typically being nearly evenly distributed.

The difference $\Delta S_2(m, t)$ can be defined as follows:

$$\Delta S_2(m, t) = \max\{S_2(m, r, t)\} - \min\{S_2(m, r, t)\} \tag{7}$$

Therefore, the local maximum time t corresponds to the zero point of $S_2(m, r, t)$ or the minimum value of $\Delta S_2(m, t)$. The time series delay τ_d is identified as the first value among the largest local times t. At this point, these maxima are nearly evenly distributed, and the reconstructed attractor is fully expanded in phase–space. Thus, the delay time τ_d is determined by the first local maximum, and the delay time τ is calculated using the formula $\tau_d = \tau\tau_s$.

When determining the embedded window τ_w, $S_2(m, r, t)$ and $\Delta S_2(m, t)$ are assumed to approach 0; thus, $S_{cor}(t)$ can be defined as the indicator as follows:

$$S_{2cor}(t) = \Delta\overline{S}_2(t) + |\overline{S}_2(t)| \tag{8}$$

The optimal estimation of the embedding window τ_w is obtained by identifying the global minimum point. Using Equation (6), the embedding dimension m can then be calculated. $\Delta\overline{S}_2(t)$ and $\overline{S}_2(t)$ are determined by averaging $S_2(m, r, t)$ and $\Delta S_2(m, t)$ for different values of m and r. Based on the statistical analysis, the range for m and r can be expressed as follows: $2 \leq m \leq 5, \frac{\sigma}{2} \leq r \leq 2\sigma$, where σ is the standard deviation of the time series.

$$\tau_w = (m-1)\tau_d \tag{9}$$

Thus, using Equations (5)–(7), the delay time τ and the embedding dimension m can be determined.

The improved C–C method [26] identifies the optimal delay τ_d by locating the first local minimum of $\Delta\overline{S}_1(t)$. Equations (3) and (5) show similar undulation patterns, and the optimal embedding window is determined at the periodic point $|\overline{S}_1(t) - \overline{S}_2(t)|$. Subsequently, the embedding dimension m is calculated using Equation (9). The advantage of the improved C–C method is its ability to clearly distinguish peaks at periodic points while attenuating high-frequency undulations, thus simplifying the selection of phase–space parameters.

2.2. Lyapunov Exponent

The Lyapunov exponent is a crucial quantitative measure employed to characterize the dynamical properties of a system. It represents the average exponential rate at which neighboring orbits converge or diverge in phase-space, which provides a quantitative description of chaotic motion and offers deep insights into the complex behaviors of dynamical systems. For high-dimensional dynamical systems, $x_{n+1} = F(x_n)$, where F is an m-dimensional map on $R^m \rightarrow R^m$, the Lyapunov exponent is defined [15] as follows:

$$\lambda_i = \lim_{n \to \infty} \frac{1}{n} \ln \left| \frac{P_i(n)}{P_0(n)} \right| \qquad i = 1, 2 \cdots m \tag{10}$$

where λ_i is the Lyapunov exponent in the direction of the main axis of the first ellipsoid and $P_i(n)$ is the length of the main axis of the first ellipsoid.

The system Lyapunov exponent is typically calculated using the small quantity method [27]. This approach involves reconstructing the phase–space of the $x_i, i = 1, 2, \cdots, N$ time series to obtain X_i, identifying the nearest neighbor X_i for each point X_j in the phase–space X_j, and then calculating the Euclidean distance between these points:

$$d_j(0) = \min \left\| X_j - X_{\hat{j}} \right\|, \left| j - \hat{j} \right| > p \tag{11}$$

where $d_j(0)$ is the initial distance from the jth point to its nearest neighbor, $\|..\|$ denotes the Euclidean norm, and p denotes the average period of the time series.

When each X_i point passes through i time steps, the distance becomes

$$d_j(i) = \left\| X_{j+i} - X_{\hat{j}+i} \right\|,$$
$$i = 1, 2 \cdots, \min(M - j, M - \hat{j}) \tag{12}$$

For each i, calculate the average value $y(i)$ of all $\ln d_j(i)$ of j:

$$y(i) = \frac{1}{q \Delta t} \sum_{j=1}^{q} \ln d_j(i) \tag{13}$$

where q is the number of non-zero elements and Δt is the evolutionary time-step growth.

Take the linear region $i - y(i)$, and fit a sequential regression curve using the least squares method. The slope of this curve represents the maximum Lyapunov exponent. If this exponent is greater than 0, the system exhibits chaotic behavior, with larger values indicating greater levels of chaos.

2.3. Correlation Dimension

The correlation dimension, a type of fractal dimension, is sensitive to the temporal dynamics of a system. Consequently, it is a valuable tool for determining the fractal dimension characteristics of time series data. By analyzing the correlation dimension, the chaotic properties of a system, as represented by its time series signals, can be effectively determined. The correlation dimension using the G–P method is calculated as follows. In the reconstructed phase-space described by Equation (1), the distance d_{ij} between two points is calculated, as detailed in [28]:

$$d_{ij} = \left| X_i - X_j \right| \tag{14}$$

A series of positive numbers ε is chosen, and for each ε, the number $N_1(\varepsilon)$ of $r_{i_j} < \varepsilon$ is calculated, defining the correlation function:

$$C(\varepsilon) = \frac{N_1(\varepsilon)}{N(N-1)} = \frac{1}{N(N-1)} \sum_{1 \le i \le j \le N} \theta(\varepsilon - d_{ij}) \tag{15}$$

where $\theta(\cdot)$ is the Heavisde step function and the association dimension D is defined when ε approaches to infinity:

$$D = \lim_{\varepsilon \to 0} \frac{\ln C(\varepsilon)}{\ln(\varepsilon)} \tag{16}$$

Create a double logarithmic plot of $\ln C \sim \ln \varepsilon$, and fit the slopes of the linear regions on this curve using the least squares method. When the slope obtained from the fit begins to stabilize with increasing embedding dimension m, the value at this point is D. A higher D indicates greater system instability.

2.4. K-Entropy

Kolmogorov entropy, also known as K-entropy, is a fundamental concept for quantifying the degree of randomness in a system's dynamics. It is a key measure that captures the variations in the state of a dynamical system, which provides a quantitative assessment of its randomness or disorder. This entropy metric provides valuable insights into the complexity and unpredictability of the system's behavior, helping researchers better understand its dynamic properties. Common methods for calculating K-entropy involve the maximum likelihood method and the correlation integral algorithm. In the maximum likelihood approach, the process examines two initially close points on different orbits; the time they remain separated before becoming spaced apart follows an exponential distribution.

$$c(b) = e^{-kb}, b = 1, 2, 3 \tag{17}$$

where k is the K-entropy and b is the number of evolution steps in phase-space required for a point, initially separated by a distance smaller than r_0, to exceed r_0 for the first time. After b evolution steps, the probability that the distance between two neighboring points is greater than r_0 is as follows:

$$p(b) = c(b-1) - c(b) = (e^k - 1)e^{-kb} \tag{18}$$

The joint probability of $b_1, b_2, \cdots b_W$ and k is obtained by randomly selecting W pairs of uncorrelated points in the phase-space:

$$\begin{aligned} p_k = p(b1, b2, \cdots bW, k) &= \prod_{i=1}^{W} p(b_i) \\ &= (e^k - 1)^W e^{(-k\sum b_i)} \end{aligned} \tag{19}$$

The maximum likelihood estimate of the K-entropy can be determined using Equation (19):

$$K = -\ln(i - \frac{1}{b}) \tag{20}$$

If $K = 0$, the system exhibits regular motion. If $K \to \infty$, the system shows random motion. If $K > 0$, the system is in chaotic motion, with larger values of K indicating greater degrees of chaos in the system.

2.5. Chaotic Attractor Phase Trajectories

A chaotic attractor is a geometric structure in phase–space that encapsulates the long-term behavioral patterns of a dynamical system. It represents the final form achieved through the temporal evolution of a system in phase–space. By analyzing this attractor, one can effectively distinguish between chaotic operation, random motion, and periodic or quasi-periodic behavior, hence gaining deep insights into the complex dynamics of the system. To reconstruct the chaotic system attractor and enable its visualization, phase-space reconstruction theory is employed to map the AE signal sequence of the sealing system into a high-dimensional space. From this high-dimensional space, the three principal vectors are extracted to construct the chaotic attractor for the unsealed system under various operating states. The first step involves calculation of the inner product matrix from the reconstructed matrix as described in Equation (1):

$$Y = X^T X \tag{21}$$

To reconstruct the matrix, using Equation (21), the eigenvalues of the inner product matrix are calculated. Then, the three largest eigenvalues are selected from the eigenvalues $\lambda_1, \lambda_2, \lambda_3$ of the inner product matrix to serve as the principal eigenvalues. Next, determine the eigenvectors that correspond to these three principal eigenvalues to serve as the principal vectors. A new projection matrix is obtained by projecting the reconstructed matrix along these three principal vectors. This projection matrix α, derived from the AE signals of the sealing system, represents the chaotic attractor matrix for the system.

$$\alpha = X[\xi 1, \xi 2, \xi 3] \tag{22}$$

2.6. Chaos Characterization Methods for AE Signals

Each AE time series is associated with a specific set of embedding dimensions and delay times. In this study, using the 0.5 s AE data from the start–stop phase of a dry gas seal as the computational time series, with calculations performed sequentially, the chaotic feature parameters are calculated. The detailed steps for characterizing the AE signals of the friction state in a dry gas seal using chaos theory are outlined as follows.

(1) Chaos assessment: The chaotic nature of the AE signal is evaluated by calculating the maximum Lyapunov exponent during the start–stop phase of the dry gas seal. This step is designed to confirm whether the signal exhibits chaotic behavior.

(2) Phase-space reconstruction: The modified C–C method is employed to simultaneously determine the optimal delay time and embedding dimension for phase-space reconstruction. This reconstruction is crucial for understanding the dynamic properties of the system.

(3) Calculation of chaotic characterization parameters: Using the small data volume method, the maximum Lyapunov exponent of the reconstructed signal is calculated. Moreover, to determine the correlation dimension of the signal, the G–P algorithm is applied, and to calculate its K-entropy, the maximum likelihood estimation method is employed. These parameters collectively reveal the chaotic nature of the system.

(4) Chaos characterization: The relationship between the three calculated parameters and the friction state of the dry gas seal is analyzed. This analysis provides a deeper understanding of how the chaotic properties relate to the friction behavior of the seals.

3. Experimental Setup

3.1. Dry Gas Seal Working Principle and Test System

This study examines the friction state of the sealing end face in a double-end-face dry gas seal, which is composed mainly of a rotating ring, stationary ring, spindle, spring, and seal seat, and its structure is depicted diagrammatically in Figure 1. On the basis of the working principle of the dry gas seal, sealing gas enters the sealing gap and, as rotational speed increases, a micrometer-thin fluid film forms between the rotating and stationary rings. During normal and stable operation of the sealing system, the moving and stationary rings are separated by a thin gas film that effectively reduces leakage while being sufficiently rigid to prevent contact between the rotating and stationary rings. Based on the Stribeck curve, the dry gas seal can experience various friction states, which include boundary lubrication (BL), mixed lubrication (ML), and hydrodynamic lubrication (HL), as shown in Figure 2. Dry gas seals operate most effectively under HL, where friction and leakage are minimized.
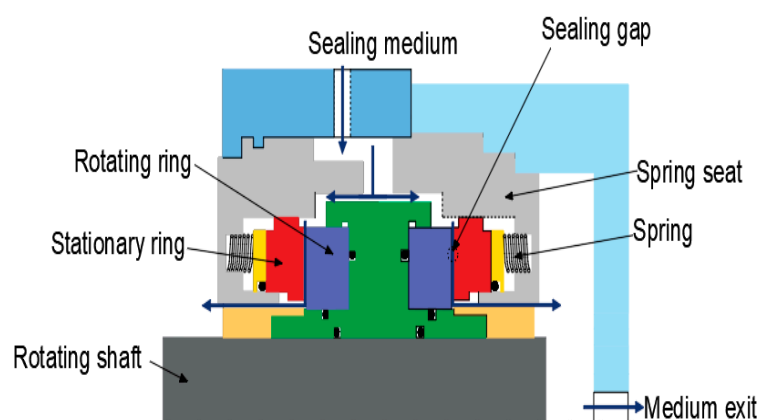
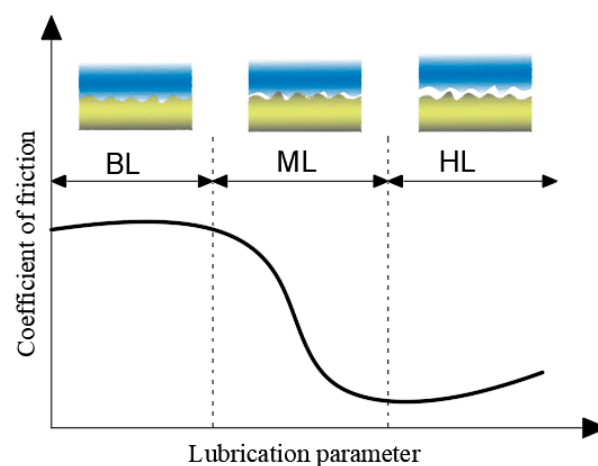**Figure 1.** Schematic diagram of dry gas seal structure.

Figure 2. Stribeck curve.

Figure 3 presents the dry gas sealing experimental bench and the AE monitoring system, which includes the main experimental unit (rotational speed range: 0–3000 r/min), an AE acquisition system, a gas circuit, a gas supply system (maximum pressure: 6 MPa), and an industrial control calculator. The AE sensor (model PXR15RMH, sampling frequency: 2 MHz) is positioned outside the seal cavity. The preamplifier utilized is PXPA3, offering a 40-dB gain, and the acquisition card is the ADLINK USB1210.
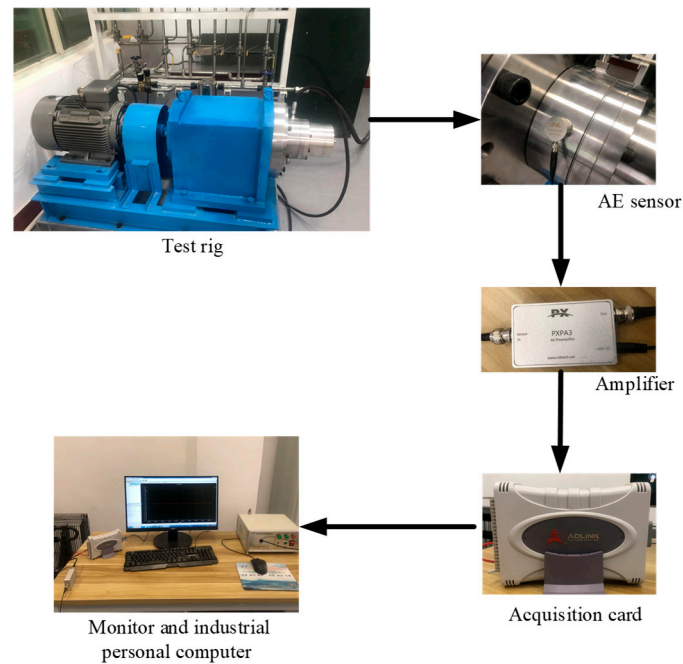
Figure 3. Overview of the dry gas sealing test bench.

This experiment employs a double-end face tree groove dry gas seal, presented in Figure 4. The rotating ring is constructed from silicon carbide, whereas the stationary ring is made of M120D. During normal and stable operation of the sealing system, the moving and stationary rings are separated by a thin gas film that effectively reduces leakage while being sufficiently rigid to prevent contact between the rotating and stationary rings.

(**a**)   (**b**)
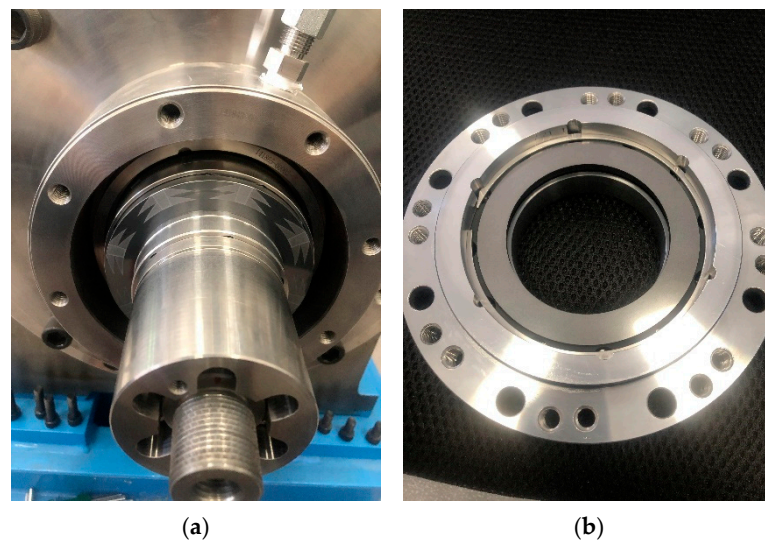
Figure 4. Physical picture of the sealing component. (**a**) Rotating ring. (**b**) Stationary ring.

3.2. Test Program

AE signals are recorded under both pressure and no-load conditions in order to gain a deeper understanding of the chaotic characteristics of the dry gas seal during the start–stop phase. With the air supply system's maximum pressure set at 6 MPa and the dry gas seal's design pressure at 3.0 MPa, experimental pressures are adjusted to 0.5, 1.0, 1.5, 2.0, 2.5, and 3.0 MPa. The low-speed test bench is employed, with the rotational speed gradually increasing from 0 to 2000 r/min during the startup process. After reaching the desired speed, the system operates stably for 5 s before being stopped. During the start–stop

process, the contact state of the sealing ring transitions from initial contact to opening and back to contact, with corresponding changes in the lubrication state. The specific steps are shown in Figure 5.
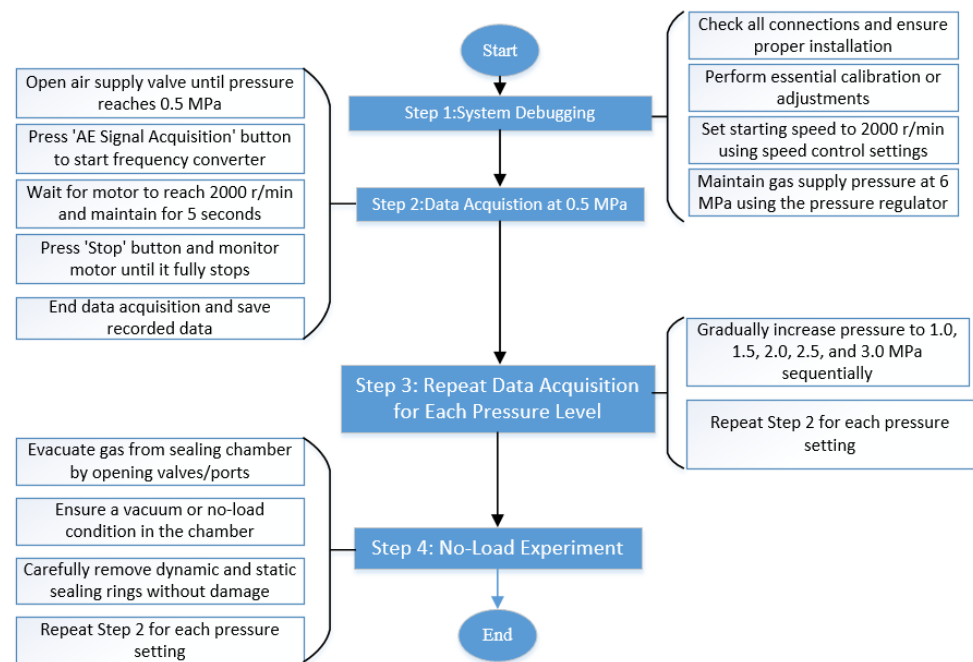

Figure 5. Test operation flow chart.

4. Results and Discussion

### 4.1. Seal End Face Friction State Analysis

Studies have shown that AE energy can be quantified using the RMS, which corresponds to the multiple interactions of the AE source mechanism in touch-grinding contact [3,13]. Hence, in this study, the RMS value is selected to analyze the AE signals of the dry gas seals. It is calculated using the following equation:

$$RMS = \sqrt{\frac{1}{\Delta T}\int_0^{\Delta T} V^2(\tau)d\tau} \tag{23}$$

where ΔT is the waveform sampling time and $V(\tau)$ is the time-varying signal voltage.

To investigate the relationship between AE energy and the contact friction state of the dry gas seal interface, the RMS value of the AE signal is employed as a substitute for AE energy. Using a working pressure of 1.0 MPa as an example, a full-cycle operation plot of RMS versus RPM is created. As shown in Figure 6, the RMS value of the dry gas seal during startup and operational states fluctuates considerably compared with the no-load signal RMS, with a peak value of 1.6 V observed during a 2–3 s duration. In other operational states, the RMS value is approximately 0.2–0.4 V, which is consistent with the no-load signal. When the dry gas seal operates normally at a pressure of 1.0 MPa, the RMS value quickly reaches a peak after the power is turned on, then decreases, and subsequently increases slowly over time, reaching a steady state by the fifth second. This transformation trend mirrors that observed in the no-load state. Figure 6 presents the relationship between AE energy and rotational speed during both normal and no-load operations of the dry gas seal. Evidently, under normal operation at 1.0 MPa, the RMS of the signal exhibits three distinct states in relation to rotational speed, particularly when the speed is below 100 r/min. The RMS of the AE signal initially increases with rotational speed. Nevertheless, in the range of 100–350 r/min, the RMS decreases as the rotational speed increases. Above 350 r/min,

the RMS starts to increase again with higher rotational speeds, following a trend similar to that observed under no-load conditions. During no-load operation, the RMS consistently increases with rotational speed, which aligns with the trend observed at higher speeds.
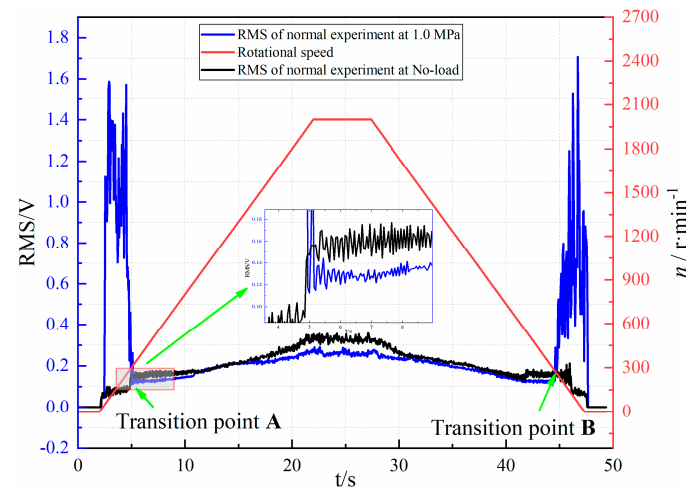
Figure 6. RMS and speed diagram of dry gas seal start–stop phase.

The working principle of dry gas seals shows that, as rotational speed increases, lubrication conditions improve, which leads to a decrease in the RMS value. A transition from the ML to the HL state occurs at point A, which corresponds to a rotational speed of 350 r/min. At this point, the sealing surface becomes fully disengaged. In Figure 7, during the initial startup phase from 0 to 100 r/min, the system is considered to be in the BL state. This occurs because, in these early stages, the dynamic pressure is insufficient to generate a rigid and stable air film. As the rotational speed increases from 100 to 350 r/min, the dynamic pressure effect progressively strengthens. At 350 r/min, the sealing ring opens to form an air film, signaling the transition from the ML to the HL state. Once the speed reaches 350–2000 r/min, the system operates normally. In this range, the dynamic pressure effect stabilizes, and the system remains in the HL state.
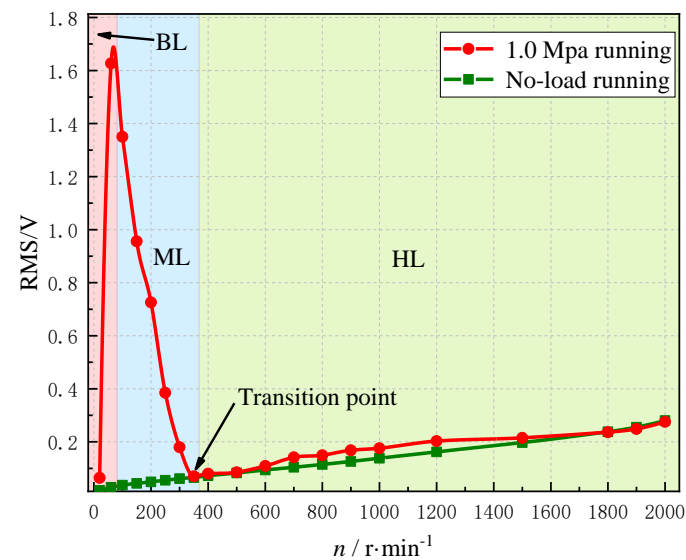

Figure 7. Trend of RMS with rotational speed in the start–stop phase.

4.2. Phase-Space Reconstruction of AE Signal During the Start–Stop Process

Using the AE signal at an operating pressure of 1.0 MPa as an example, the phase-space reconstruction parameters for the AE signals of the dry gas seal in the BL, ML, and

HL states are calculated using the improved C–C method. The results of these calculations are shown in Figure 8.
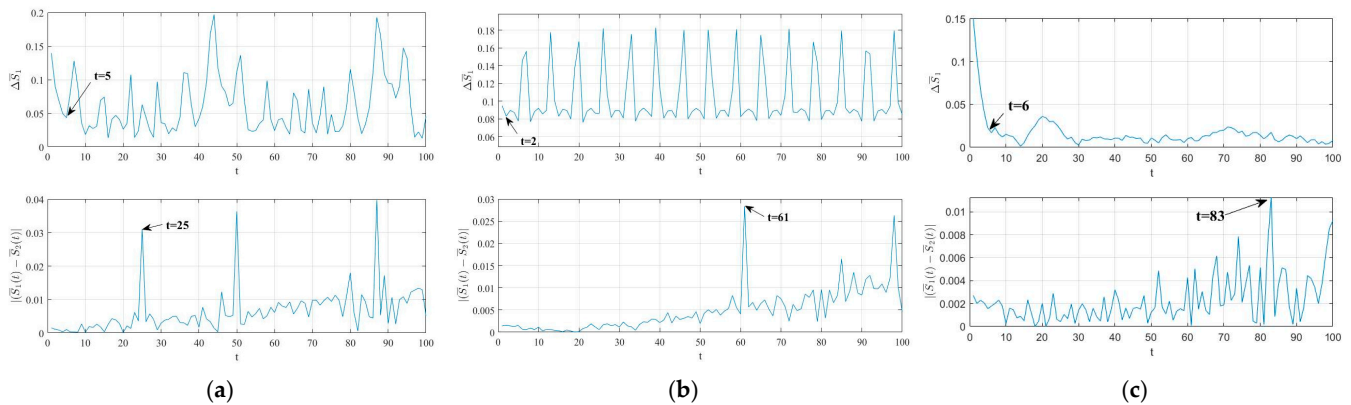
Figure 8. Calculation results for the improved C–C method at different states. (**a**) BL state. (**b**) ML state. (**c**) HL state.

To reconstruct the phase-space of the time series, the optimal time delay τ and time window τ_w are determined using Equations (3) and (5). The local minima are visible as sharp peaks in Figure 8. The embedding dimension m is calculated using Equation (9). Figure 8a shows the time delay $\tau = 5$, time window $\tau_w = 25$, and embedding dimension $m = 6$ based on Equation (6). Likewise, Figure 8b shows $\tau = 2$ and the time window $\tau_w = 61$, corresponding to $m = 32$. Figure 8c shows $\tau = 6$ and the time window $\tau_w = 83$, corresponding to $m = 15$. Using this approach, the optimal delay time τ and embedding dimension m are also calculated for other AE sequences.

4.3. Maximum Lyapunov Exponent Analysis

Figure 9 shows the AE signals for the three states of the sealing system at an operating pressure of 1.0 MPa. Using the small data volume method, the maximum Lyapunov exponent for each state is calculated. The slope of the red line in Figure 10 represents the maximum Lyapunov exponents for each state, which are 0.0123, −0.0682, and −0.1074, respectively. The positive values of the maximum Lyapunov exponents for the BL state indicate that the AE signals in this state exhibit chaotic characteristics, with the level of chaos increasing gradually over time. Upon transitioning to the ML state, the maximum Lyapunov exponent becomes negative immediately and then increases gradually over time. In the HL state, the maximum Lyapunov exponent fluctuates around the X-axis and remains below 0. Figure 10a–f shows the maximum Lyapunov exponents at pressures of 0.5, 1.0, 1.5, 2.0, 2.5, and 3.0 MPa, respectively. The fluctuation trends are similar across these pressures, which indicates that pressure has minimal impact on the maximum Lyapunov exponent.

From the AE data collected at six different pressures, 10 groups of data were selected for each friction state period. With the resulting average value representing the maximum Lyapunov exponent for each friction state, the Lyapunov exponents for these data sets were calculated and averaged. As shown in Table 1, the maximum Lyapunov exponent for the BL state of the dry gas seal is greater than 0. This shows that the chaotic characteristics of the signal in the BL state are due to the contact at the seal ring end-face, as explained by the working principle of the dry gas seal. For the ML state, the maximum Lyapunov exponent ranges from −0.0123 to 0.0022. In the ML state, the sealing ring intermittently contacts and separates due to increasing rotational speed and enhanced dynamic pressure effects. These factors cause the sealing end face to disengage, but the instability of the air film results in intermittent contact with the sealing ring, leading to a maximum Lyapunov exponent that fluctuates between positive and negative values. In the HL state, the maximum Lyapunov

exponent is consistently less than 0. This indicates that the sealing rings are completely disengaged, preventing the generation of chaotic signals, such as dry friction and contact wear. Consequently, the AE signals do not exhibit chaotic characteristics in the HL state.
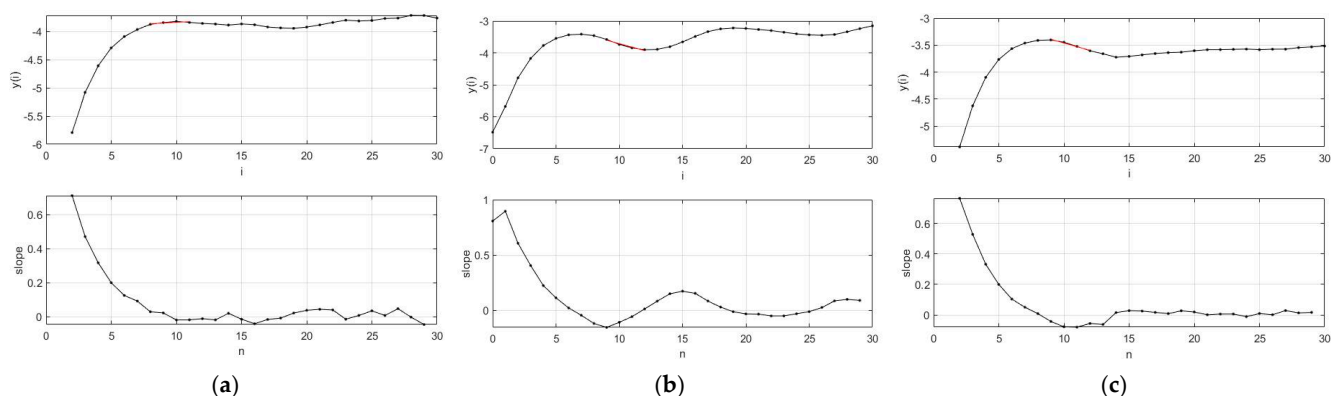

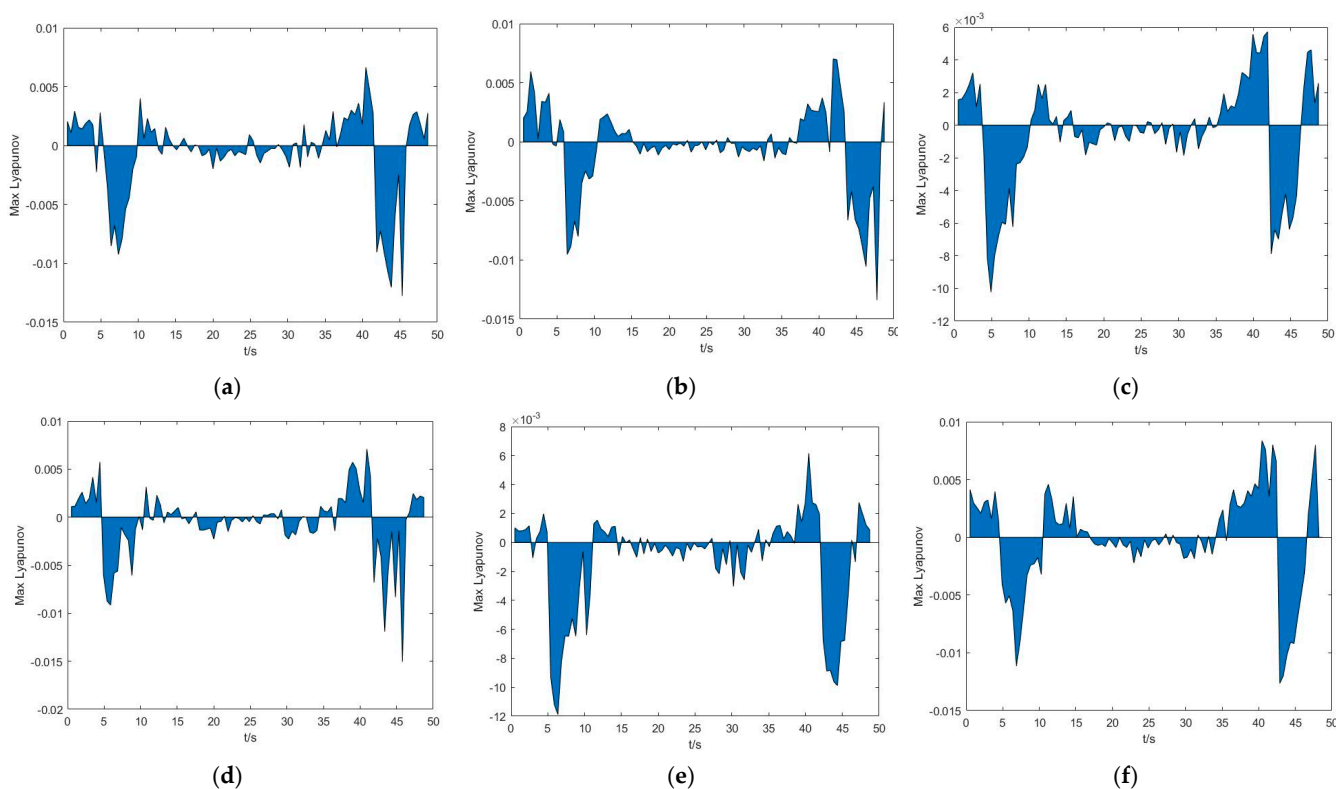**Figure 9.** Maximum Lyapunov exponent for each state at 1.0 Mpa. (**a**) BL state. (**b**) ML state. (**c**) HL state.

Figure 10. Maximum Lyapunov exponent at different pressures. (**a**) 0.5 MPa. (**b**) 1.0 MPa. (**c**) 1.5 MPa. (**d**) 2.0 MPa. (**e**) 2.5 MPa. (**f**) 3.0 MPa.

Table 1. Relationship between the friction state of the dry gas seal and the maximum Lyapunov exponent.

Friction State	Maximum Lyapunov Exponent Distribution Range
BL state	0.0021~0.0063
ML state	−0.0123~0.0022
HL state	−0.0020~0

Notably, due to the interference of ambient noise and experimental errors in the sealing system, there are periods when the maximum Lyapunov exponent is greater than 0 in the HL state, but these errors are acceptable and do not affect the overall trend.
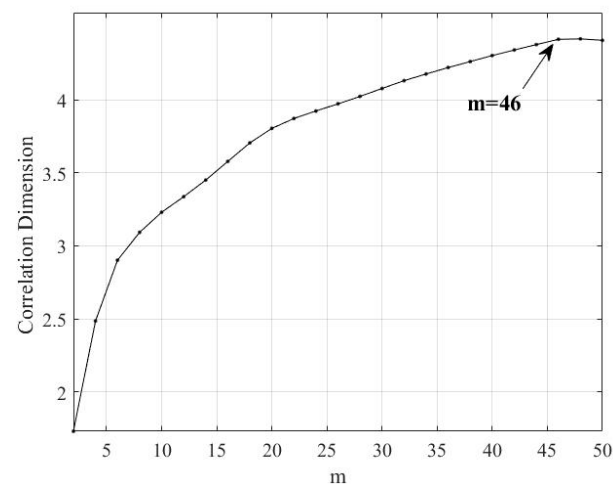
4.4. Correlation Dimension Analysis

Using the AE signal from the friction state of the seal boundary as an example, the $\ln C \sim \ln \varepsilon$ double logarithmic curve is plotted while calculating the correlation dimension using the G–P algorithm, as depicted in Figure 11.
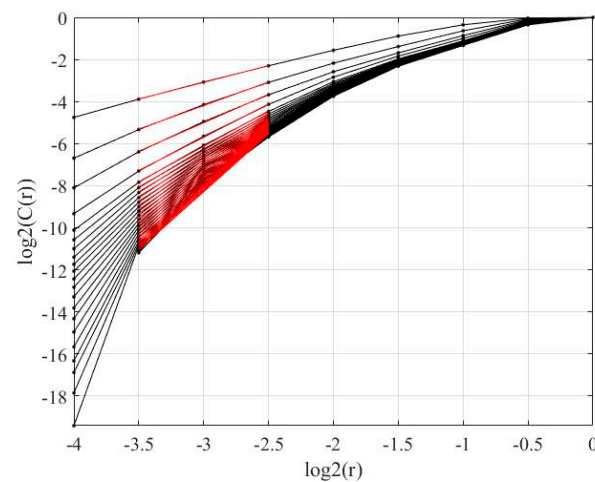
**Figure 11.** Calculation results of the G-P algorithm in the BL phase.

As shown in Figure 12, the graph plots the correlation dimension versus the embedding dimension. The correlation dimension increases as the embedding dimension increases. When the embedding dimension is $m= 46$, the correlation dimension stabilizes. For the AE time series in the BL state of the sealing system, the correlation dimension is $D= 4.426$.

**Figure 12.** Variation of correlation dimension with embedding dimension in the BL state.

The correlation dimension for each state of the sealing system can be calculated accordingly. For example, as shown in Figure 13, the correlation dimension is calculated with the G–P algorithm using AE signals from the entire start–stop process at working pressures of 0.5, 1.0, 1.5, 2.0, 2.5, and 3.0 MPa. In both the BL and ML states, the correlation dimension increases over time and reaches a peak value. In the HL state, however, the correlation dimension suddenly decreases and fluctuates between 3 and 5.5. During the

stopping state of the sealing system, the correlation dimension initially decreases and then increases, reaching a trough at the state transition point B.
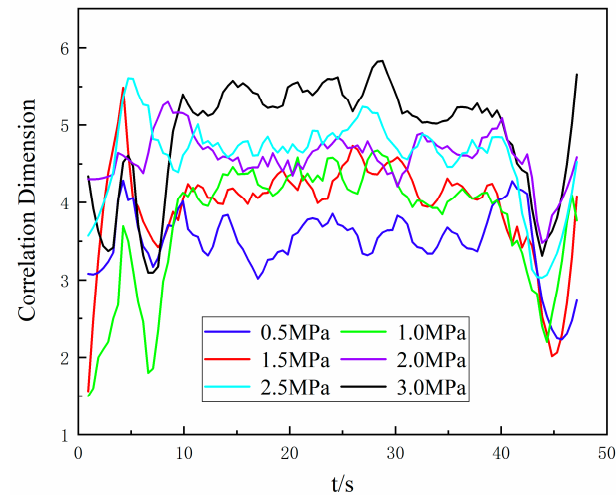
**Figure 13.** Trend in correlation dimension at various pressures.

To generate Figure 14, the average correlation dimensions for each lubrication state are compared across different pressures. In the order of BL, ML, and HL states, the correlation dimensions exhibit an increasing trend with pressure. Specifically, the correlation dimension is highest in the HL state and lowest in the BL state. As pressure increases, the correlation dimension in each state gradually increases.
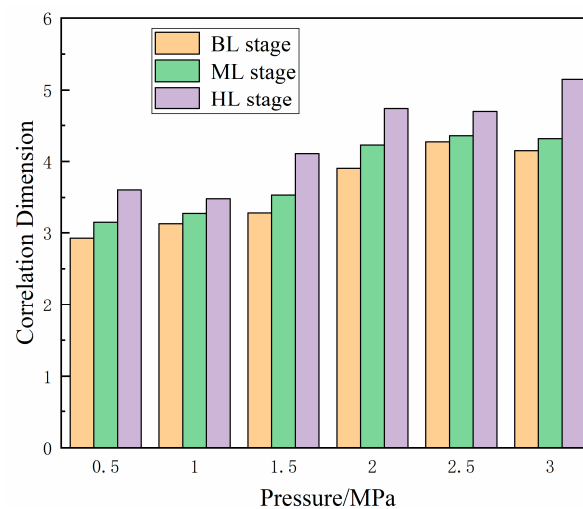
**Figure 14.** Comparison of association digits in various states.

4.5. Comparison of Association Digits in Various States

As shown in Figure 15, using the maximum likelihood method, the K-entropy of the AE signal time series in the BL state of the sealing system is calculated. For example, in the BL state, the K-entropy value decreases as the embedding dimension increases and eventually stabilizes when the embedding dimension $m > 22$. At this point, the K-entropy of the AE time series in the BL state is 0.0083.
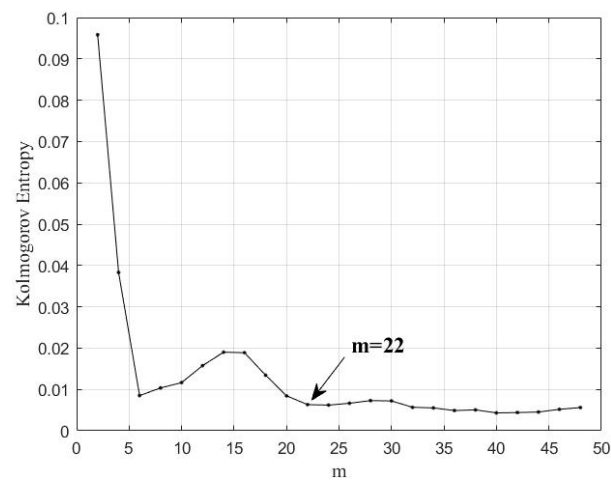
Figure 15. Variation of K-entropy with embedding dimension in the BL state.

Likewise, the K-entropy of the AE time series can be calculated for each pressure condition. The trends observed at 0.5, 1.0, 1.5, 2.0, 2.5, and 3.0 MPa are shown in Figure 16. In both the BL and ML states, K-entropy increases considerably, which indicates increasing chaotic characteristics and complexity. In the HL state, K-entropy initially decreases and then increases with rising rotational speed during the startup process and decreases before increasing again as the rotational speed drops during the stopping phase. During the stopping process, K-entropy decreases as the rotational speed in both the ML and BL states decreases.
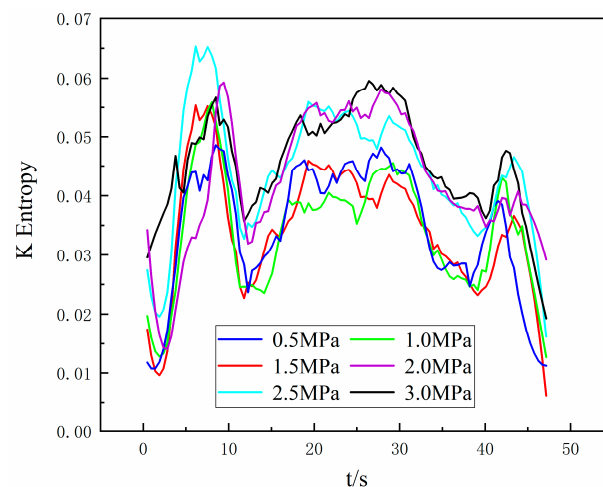

Figure 16. Trend of K-entropy at different pressures.

In terms of the friction mechanism, in the BL and ML states, the dry gas seal provides insufficient dynamic pressure at low speeds, which results in abrasive contact on the sealing end face. This leads to increased AE activity, with corresponding increases in the maximum Lyapunov exponent, correlation dimension, and K-entropy. In the HL state, the sealing end face is fully disengaged, eliminating the abrasive contact. Consequently, the maximum Lyapunov exponent, correlation dimension, and K-entropy experience a sharp decrease, stabilizing at a lower level as the rotational speed increases. During the stopping phase, as the system transitions back to ML and BL states, the maximum Lyapunov exponent reflects these changes, and correlation dimension and K-entropy decrease with the decrease in rotational speed.

The K-entropy values for each state at various pressures are averaged and depicted in Figure 17. For instance, at 1.5 MPa, the BL state exhibits the lowest K-entropy value,

whereas the HL state shows the highest value. Moreover, it is observed that pressure has only a minor effect on the K-entropy values at different states.
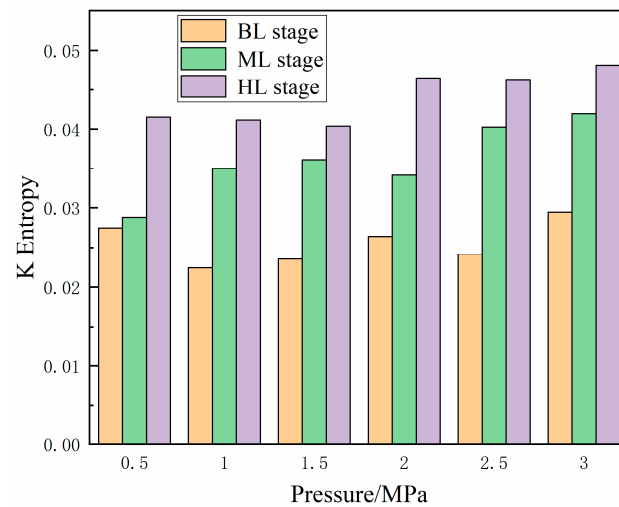

Figure 17. Comparison of K-entropy at various states.

4.6. Changes in Attractors

Using the AE signal of the 1.0 MPa sealing system as an example, Figures 18–20 show the evolution of chaotic attractors across three states. In the BL state (Figure 18), the chaotic attractor appears agglomerated and concentrated, with amplitude variations in the *X*, *Y*, and *Z* directions in the range of [−5, 5]. In the ML state (Figure 19), the attractors change from a "clustered" configuration to one that is centered with dispersion on the surface, with amplitude changes in the *X*, *Y*, and *Z* directions in the range of [−1, 1]. In the HL state (Figure 20), the attractor is fully diffused, and amplitude variations in the *X*, *Y*, and *Z* directions are in the range of [−2, 2].
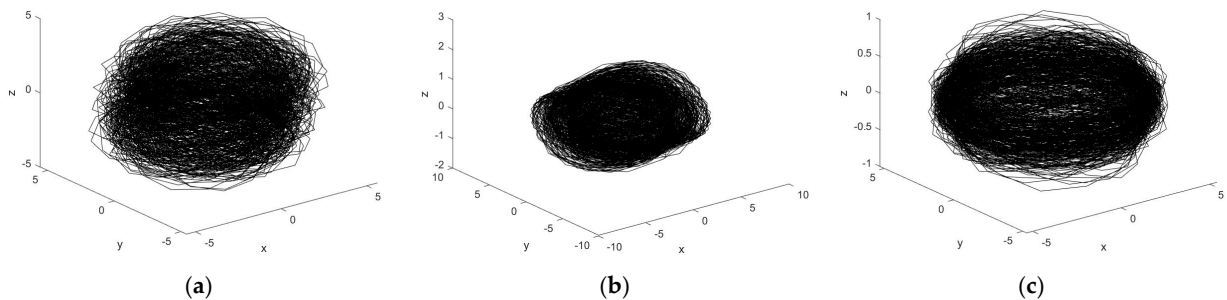
Figure 18. Evolution diagram of the attractor in the BL state. (**a**) at 2.1 s. (**b**) at 2.2 s. (**c**) at 2.3 s.
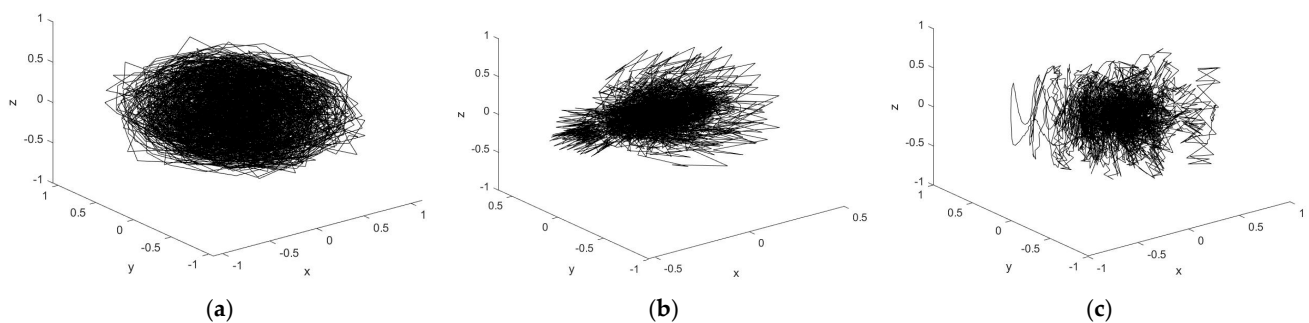
Figure 19. Evolution diagram of the attractor in the ML state. (**a**) at 3.0 s. (**b**) at 3.2 s. (**c**) at 3.4 s.
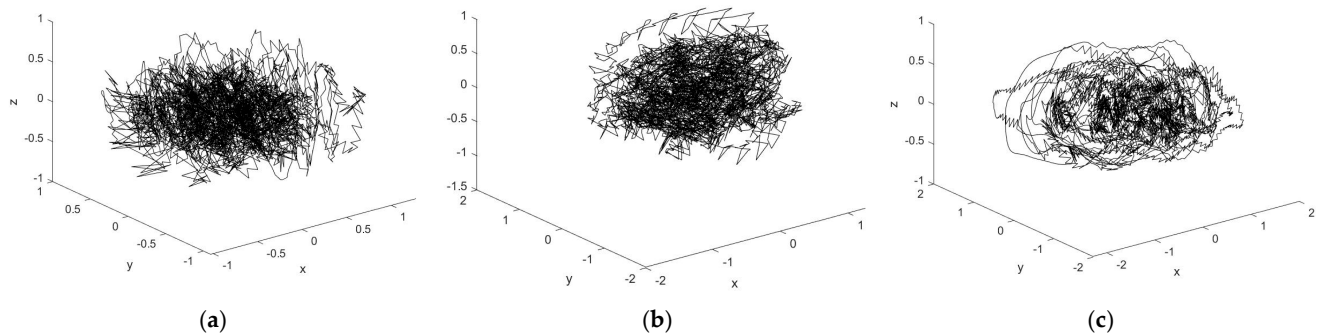
Figure 20. Evolution diagram of the attractor in the HL state (**a**) at 7.0 s. (**b**) at 12.0 s. (**c**) at 18.0 s.

From the perspective of friction mechanisms, in the BL state, the presence of dry friction and surface wear on the seal end face increases the chaos in the AE signal, which results in dense attractors with higher amplitude. In the ML state, as dry friction and friction force decrease, the AE energy continues to decrease, leading to a gradual dispersion of the attractors. In the HL state, with the absence of dry friction and a stabilized sealing system, the AE signal lacks chaotic characteristics, and the attractors become fully dispersed.

In summary, analyzing the chaotic characteristics of the AE signal from the dry gas seal shows that the maximum Lyapunov exponent is a crucial metric for determining the friction state. Specifically, a maximum Lyapunov exponent greater than 0 indicates that the system is in the BL state. Conversely, a lower value suggests that the system is in the HL state. A transition from a negative to a positive maximum Lyapunov exponent, along with a decrease in its value, depicts the ML state. The correlation dimension and K-entropy show similar trends, providing a broader perspective on assessing the friction state of the dry gas seal. In the HL state, the characteristic parameters show relative stability whereas, in the BL state, they generally increase and, in the ML state, they present a decreasing trend. Moreover, the attractor's dynamic behavior offers an intuitive way to assess the system's state. A regular clustering pattern of the attractors indicates the BL state, whereas a central clustering with surface divergence characterizes the ML state. Complete diffusion of the attractor indicates the HL state. Thus, the attractor provides a complementary method for determining the friction state of the dry gas seal, enhancing the analysis derived from chaotic characteristic parameters.

4.7. Performance Comparison

To further validate the effectiveness of the method presented in this paper, the same AE data were processed to determine recognition accuracies for different friction states, as depicted in Table 2. The results in Table 2 show that the method achieved satisfactory results in identifying the friction states of the dry gas seal. Notably, Huang et al. [10] and Sun et al. [12] reported the lowest detection accuracy using the RMS method. This method primarily reflects the contact conditions of the seal end face and is less effective in distinguishing the intermittent contact and non-contact scenarios typical of the ML state. Xu et al. [11] determined different friction states based on the amplitude of the AE signal, which is prone to interference from external noise and offers limited improvements in detection accuracy. Towsyfyan et al. [13] employed the three-dimensional short-time Fourier time–frequency diagram method, which offers high detection accuracy. However, this method requires analysis of the entire start–stop process and cannot identify the friction state of a specific section of the AE signal alone. In comparison, the maximum Lyapunov exponent method proposed in this paper effectively detects the sealing system's friction state with an average accuracy of 98.6%. Furthermore, the correlation dimension and K-entropy methods achieve accuracies of 96.9% and 96.5%, respectively.

Table 2. Detection accuracy for different friction states.

Method/Friction States	BL	ML	HL	Average
Huang et al. [10]	89.2%	89.1%	95.9%	91.3%
Xu et al. [11]	95.3%	91.0%	93.2%	93.2%
Sun et al. [12]	90.7%	88.8%	90.3%	89.9%
Towsyfyan et al. [13]	96.2%	97.2%	98.3%	97.2%
Maximum Lyapunov	98.3%	98.8%	98.8%	98.6%
Correlation dimension	97.6%	96.3%	96.9%	96.9%
K-entropy	96.2%	96.3%	97.0%	96.5%

Table 3 presents the computational speeds of various methods, indicating that the method proposed in this study has relatively low computational speed. However, this approach achieves considerable improvements in detection accuracy, which is advantageous in practical applications. The results reveal that the proposed method is highly effective for monitoring the friction and lubrication status of dry gas seals.

Table 3. Detection speed for different friction states.

Method/Friction States	BL	ML	HL	Average
Huang et al. [10]	13 s	14 s	15 s	14 s
Xu et al. [11]	18 s	17 s	17 s	17 s
Sun et al. [12]	20 s	22 s	23 s	21 s
Towsyfyan et al. [13]	160 s	162 s	161 s	161 s
Maximum Lyapunov	153 s	156 s	160 s	156 s
Correlation dimension	140 s	145 s	141 s	142 s
K-entropy	112 s	118 s	120 s	117 s

5. Conclusions

(1) The maximum Lyapunov exponent provides a precise quantitative measure for identifying the friction state of dry gas seals, while the correlation dimension and K-entropy offer qualitative insights into the system's behavior. This integrated approach facilitates a comprehensive evaluation and optimization of seal performance.

(2) Comparisons of the correlation dimension, maximum Lyapunov exponent, and K-entropy under varying pressure conditions indicate that pressure variations have minimal influence on these characteristic metrics.

(3) The chaotic properties of the sealing system can be intuitively visualized through attractor trajectories, providing a clear method to distinguish between different friction states.

(4) Chaotic time series analysis of AE signals during the start–stop phase reveals that the correlation dimension, maximum Lyapunov exponent, and K-entropy exhibit consistent trends and correlate directly with the friction state. These metrics serve as reliable indicators for identifying friction states, offering a novel approach to state recognition and fault detection in dry gas seals. This comprehensive analysis sheds new light on the dynamic behavior of seals during the start–stop process, enhancing the understanding and monitoring of their performance.

Author Contributions: Conceptualization, S.Z. and J.C.; Data curation, S.Z.; Investigation, S.W.; Methodology, X.D.; Resources, J.C.; Formal analysis, L.Z.; Writing—original draft, S.Z.; Writing—review and editing, S.Z. All authors will be updated at each stage of manuscript processing, including submission, revision, and revision reminder, via emails from our system or the assigned Assistant Editor. All authors have read and agreed to the published version of the manuscript.

References

1. Wang, Y.; Yang, H.; Wang, J.; Liu, Y.; Wang, H.; Feng, X. Theoretical analyses and field applications of gas-film lubricated mechanical face seals with herringbone spiral grooves. *Tribol. Trans.* **2009**, *52*, 800–806. [CrossRef]

2. Reddyhoff, T.; Dwyer-Joyce, R.S.; Harper, P. A New Approach for the Measurement of Film Thickness in Liquid Face Seals. *Tribol. Trans.* **2008**, *51*, 140–149. [CrossRef]

3. Towsyfyan, H.; Gu, F.; Ball, A.D.; Liang, B. Modelling acoustic emissions generated by tribological behaviour of mechanical seals for condition monitoring and fault detection. *Tribol. Int.* **2018**, *125*, 46–58. [CrossRef]

4. Haisheng, B.I.; Zili, L.I.; Dedong, H.U. Cluster analysis of acoustic emission signals during tank bottom steel pitting corrosion process. *J. China Univ. Pet. (Ed. Nat. Sci.)* **2015**, *39*, 145–152.

5. Orcutt, F.K. An investigation of the operation and failure of mechanical face seals. *J. Tribol.* **1969**, *91*, 713. [CrossRef]

6. Miettinen, J.; Siekkinen, V. Acoustic emission in monitoring sliding contact behaviour. *Wear* **1995**, *181*, 897–900. [CrossRef]

7. Mba, D.; Roberts, T.; Taheri, E.; Roddis, A. Application of acoustic emission technology for detecting the onset and duration of contact in liquid lubricated mechanical seals. *Insight-Non-Destr. Test. Cond. Monit.* **2006**, *48*, 486–487. [CrossRef]

8. Patil, A.P.; Mishra, B.K.; Harsha, S.P. Vibration based modelling of acoustic emission of rolling element bearings. *J. Sound Vib.* **2020**, *468*, 115117. [CrossRef]

9. Zhang, Y.; Lu, W.; Chu, F. Planet gear fault localization for wind turbine gearbox using acoustic emission signals. *Renew. Energy* **2017**, *109*, 449–460. [CrossRef]

10. Huang, W.; Lin, Y.; Liu, Y.; Liu, X.; Gao, Z.; Wang, Y. Face rub-impact monitoring of a dry gas seal using acoustic emission. *Tribol. Lett.* **2013**, *52*, 253–259. [CrossRef]

11. Xu, L.; Wu, J.H.; Yuan, X.; Hao, M.; Liu, F.; Liu, Y.; Xie, X. Influence of inlet pressure disturbance on transient performance of liquid oxygen lubricated mechanical seal and rub-impact phenomenon caused by excitation overload. *Tribol. Int.* **2023**, *178*, 108058. [CrossRef]

12. Sun, X.; Zheng, X.; Xu, P.; Liu, H.; Tian, J.; Wang, Z.; Hao, M. Research on friction state monitoring method of liquid film seal during start-up based on acoustic emission. *Appl. Acoust.* **2023**, *210*, 109424. [CrossRef]

13. Towsyfyan, H.; Gu, F.; Ball, A.D.; Liang, B. Tribological behaviour diagnostic and fault detection of mechanical seals based on acoustic emission measurements. *Friction* **2019**, *7*, 572–586. [CrossRef]

14. Li, X.; Fu, P.; Chen, K.; Lin, Z.; Zhang, E. The contact state monitoring for seal end faces based on acoustic emission detection. *Shock Vib.* **2016**, *1*, 8726781. [CrossRef]

15. Zhu, H.; Ge, S. Chaotic properties of tribological systems. *J. Mech. Eng.* **2004**, *40*, 10–13. [CrossRef]

16. Sun, D.; Li, G.; Wei, H.; Liao, H. Experimental study on the chaotic attractor evolvement of the friction vibration in a running-in process. *Tribol. Int.* **2015**, *88*, 290–297. [CrossRef]

17. Lewis, M.J.; Short, A.L.; Suckling, J. Multifractal characterisation of electrocardiographic RR and QT time-series before and after progressive exercise. *Comput. Methods Programs Biomed.* **2012**, *108*, 176–185. [CrossRef]

18. Ziaja, A.; Antoniadou, I.; Barszcz, T.; Staszewski, W.J.; Worden, K. Fault detection in rolling element bearings using wavelet-based variance analysis and novelty detection. *J. Vib. Control* **2016**, *22*, 396–411. [CrossRef]

19. Takens, F. Detecting strange attractors in turbulence. In *Dynamical Systems and Turbulence, Warwick*; Springer: Berlin/Heidelberg, Germany, 1981; pp. 366–381.

20. Kantz, H.; Schreiber, T. *Nonlinear Time Series Analysis*; Cambridge University Press: Cambridge, UK, 2003.

21. Fraser, A.M.; Swinney, H.L. Independent coordinates for strange attractors form time series. *Phys. Rev. A* **1986**, *33*, 1134–1140. [CrossRef]

22. Grassberger, P.; Procaccia, I. Measuring the strangeness of strange attractors. *Phys. D Nonlinear Phenom.* **1983**, *9*, 189–208. [CrossRef]

23. Pratap Mukherjee, R.; Kumar Roy, P.; Kumar Pradhan, D. An Efficient FNN model with chaotic oppositional based SCA to solve classification problem. *IETE J. Res.* **2023**, *69*, 4205–4223. [CrossRef]

24. Hajiloo, R.; Salarieh, H.; Alasty, A. Chaos control in delayed phase space constructed by the Takens embedding theory. *Commun. Nonlinear Sci. Numer. Simul.* **2018**, *54*, 453–465. [CrossRef]

25. Kim, H.; Eykholt, R.; Salas, J.D. Nonlinear dynamics, delay times, and embedding windows. *Phys. D Nonlinear Phenom.* **1999**, *127*, 48–60. [CrossRef]

26. Lu, Z.B.; Cai, Z.M.; Jiang, K.Y. Phase Space Reconstruction Parameter Selection Based on improved CC Method. *J. Syst. Simul.* **2007**, *11*, 2527–2529.

27. Lang, S.H.; Zhu, H.; Wei, C.L. Study on the boundedness, stability and dynamic characteristics of friction system based on fractal and chaotic theory. *Tribol. Int.* **2023**, *180*, 108228. [CrossRef]

28. Zhou, Y.; Zhu, H.; Zuo, X.; Yang, J. Chaotic characteristics of measured temperatures during sliding friction. *Wear* **2014**, *317*, 17–25. [CrossRef]